Hindawi
Advances in Civil Engineering
Volume 2018, Article ID 9841374, 15 pages
https://doi.org/10.1155/2018/9841374

Research Article

The Influence of Heading Rate on Roof Stability in Coal Entry Excavation

Sen Yang,[1,2] **Nong Zhang**,[1] **Xiaowei Feng**,[1] **Dongjiang Pan**,[1] **and Deyu Qian**[1]

[1] *Key Laboratory of Deep Coal Resource Mining, Ministry of Education of China, School of Mines, China University of Mining & Technology, Xuzhou 221116, China*
[2] *Department of Energy and Mineral Engineering, G3 Center and Energy Institute, The Pennsylvania State University, University Park, PA 16802, USA*

Correspondence should be addressed to Sen Yang; yangsen2009@outlook.com

Received 19 February 2018; Revised 16 April 2018; Accepted 14 July 2018; Published 29 August 2018

Academic Editor: Prodromos Psarropoulos

Coal entry heading is one of the most hazardous activities in coal mine operations because a certain area of an unsupported roof inevitably forms and poses a significant threat to the safety of miners. In order to accelerate the coal entry heading, a simplified method including theoretical analysis and laboratory and in situ tests was developed to predict the influence of heading rate on the stability of the unsupported immediate roof. The results demonstrate that the deflection of the unsupported immediate roof at the heading face is on a scale of millimetre; hence, monitoring the deformation by conventional observation methods is difficult. The proposed model shows that, within the unsupported immediate roof, the peak values of normal stresses σ_x (perpendicular to the direction of excavation) and σ_y (parallel to the direction of excavation) and shear stresses τ_{xz} (perpendicular to the direction of excavation) and τ_{yz} (parallel to the direction of excavation) have different changing trends. The peak values of σ_x and σ_y both rise with the increasing advancing distance; however, σ_y reaches the tensile strength within a shorter range than σ_x. Moreover, the peak values of τ_{xz} and τ_{yz} initially increase with the increasing advancing distance and then stabilize or decline. The major threat to roof stability at the heading face is tensile failure parallel to the heading direction. According to the industry practices, it is proved that our method can make a good prediction of the mechanical state of the unsupported immediate roof, further deriving the heading rate with a considerable safety margin.

1. Introduction

As the biggest coal-producing and -consuming country in the world, more than 70% of China's energy is provided by burning coal [1, 2]. Longwall mining is the main coal-extracting method used in China, with over 85% of the coal produced by longwall mining. Since the 1990s, with the development of mechanized coal mining, the "super long-wall panel" that can produce 1–10 million tonnes of raw coal per year has been commonly implemented in China. With this technology, the advancing rate of a longwall panel can exceed 3000 m/year [3, 4] and will continue to increase. The rapidly advancing longwall panel will inevitably destroy a large part of the coal entry. Therefore, to avoid expensive production interruptions, Chinese coal mine managers and engineers are examining ways to apply the highly efficient heading of coal entry.

Highly efficient heading can be achieved by balancing speed with safety. In China, the most common heading technique utilizes a roadheader combined with a roof bolter (Figure 1). After excavating an advancing distance L_0, the roadheader retreats about 5 m from the coal face; then, the roof bolter is moved close to the coal face, and the miners insert bolts into the rock to support the newly exposed roof. This frequent position exchange is time-consuming and reduces the heading speed greatly. Although increasing L_0 can lower the frequency of the operation, it increases the risk that the longer unsupported roof will trigger roof collapse which poses a hazard to miners and equipment. Therefore, for highly efficient coal entry heading, we need to know the

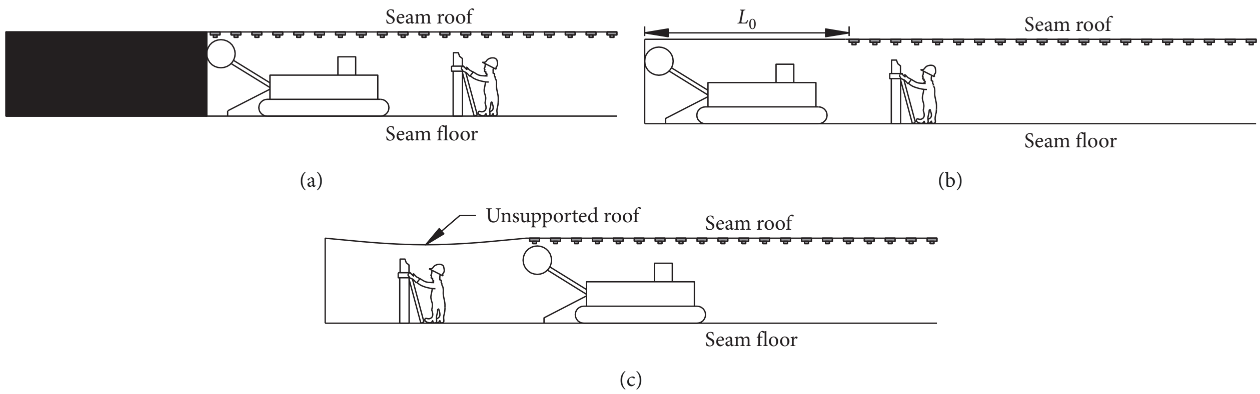

Figure 1: Heading technique consisting of the roadheader and roof bolter. (a) Roadheader starts to excavate. (b) Roadheader finishes a cycle of excavation. (c) The roof bolter is moved close to the coal face to support the newly exposed roof.

safe advancing distance L_0 that can maintain roof stability as the roadheader moves forward.

Extensive investigation was conducted to prevent roof collapses in underground coal mines. Several geotechnical variables that affect roof stability have been identified. These include the geology, mine opening geometry, horizontal and vertical stress regime, abutment pressure, and support [5–12]. Most studies of mine roof stability try to determine the relationship between roof failures and the abovementioned variables by using statistical analysis [13–19]. The detailed measurements help us understand the mechanics of roof instability and failure; however, the stratigraphy around coal mines can be complex, and the mining parameters vary between mines. Hence, the results of the above studies may be site-specific and not applicable to other mines.

Although the stability of the unsupported roof near the heading face is a vital factor for mining engineers when considering increasing the heading rate and preventing roof collapse, few studies have investigated this issue in depth. Hence, in this study, we develop an accurate model to predict the mechanical behavior of the unsupported roof. To improve the performance and effectiveness of the constructed model, a series of tests are conducted to obtain the parameters used in the model. The model is applied to a real coal excavation case, verifying its reliability as a tool for increasing mining safety and achieving highly efficient heading operation.

2. Problem Definition

The bearing structure of a typical heading face is illustrated in Figure 2. After excavation, the strong main roof supports the overlaying strata and maintains self-stability. Below the main roof, the weak strata (usually mudstone or siltstone) bend downward, causing separation of the weak strata from the main roof. At this stage, most of the weak strata are supported by the immediate roof. Hence, excavation-induced roof failure will initially begin at the immediate roof surface where the stress is concentrated and then will propagate upward into the deeper roof. This causes a huge loss of bearing capacity at the immediate roof and increases the likelihood of triggering roof collapse. Thus, the roof stability near the heading face is directly related to the stress regime and the engineering characteristics of the immediate roof.

The unsupported immediate roof can be simplified as a rectangular plate model (Figure 3) whose three edges are hinged at the rock stratum and one edge is hinged at the row of bolts next to the heading face. Previous studies generally regarded the area of the plate as the area of the exposed roof [20–24]. This conception assumes that the coal ribs are rigid. However, in fact, the coal seam is much weaker than the roof and floor. The entry excavation causes the initial failure of the shallow coal rib, and it will gradually extend to the deep coal body. Hou and Ma [25] proposed a mechanical model (Figure 4) to calculate the normal stress distribution in the coal-roof interface of a coal rib. The model results indicate that the shallow coal rib loses most of its bearing capacity due to failures. This increases the area of the unsupported immediate roof. Therefore, in this work, the mechanical model (Figure 3) takes into account the roof over the broken coal rib.

The normal stress σ_z is obtained by

$$\sigma_z = \left(\frac{C_0}{\tan\varphi_0} + \frac{P_s}{A}\right)\exp\left(\frac{2\tan\varphi_0}{MA}\alpha\right) - \frac{C_0}{\tan\varphi_0}, \tag{1}$$

where σ_z is the normal stress of the limit equilibrium zone in the coal rib; C_0 is the cohesion of the coal rib; φ_0 is the internal friction angle of the coal rib; P_s is the support resistance at the coal-rib edge; A is the ratio of horizontal stress to vertical stress that can be obtained by in situ measurements; M is the thickness of the coal seam. In Figure 4, α_0 is the width of the limit equilibrium zone; H is the mining depth; γ is the average unit weight of the overlying strata which can be obtained by in situ measurements; and k is the stress concentration factor, and the proposed value is 2 [25].

A realistic value for the width of the broken coal rib (l in Figure 4) is important for ensuring that the analysis returns valid results, but there is almost no reported in situ compressive test on coal ribs. Nevertheless, available results of extensive in situ compressive tests on coal pillars can provide valuable information for our modeling. Three sets of existing data on large-scale coal tests collected from References

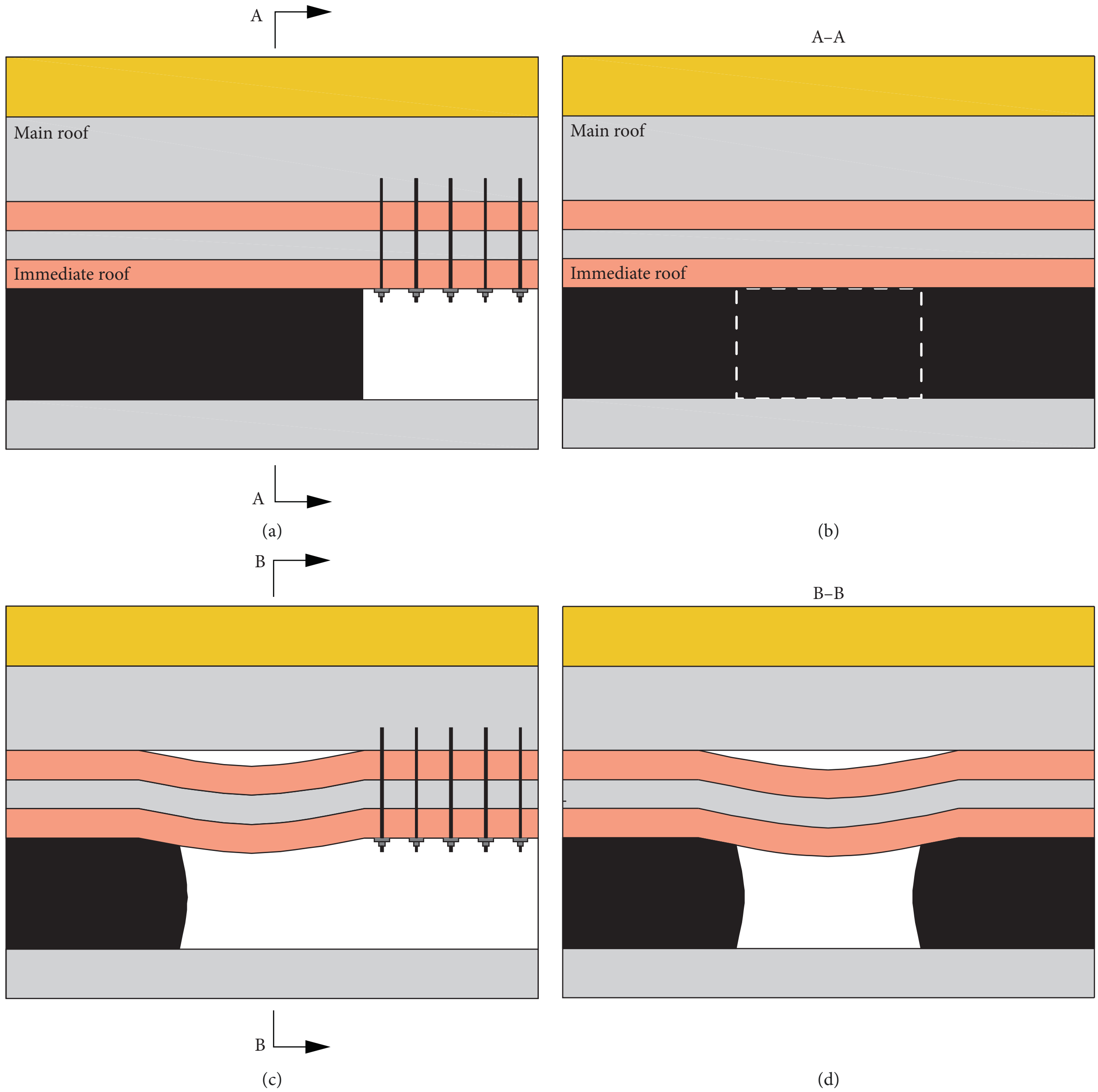

Figure 2: Bearing structure near a typical heading face in coal entry excavation. (a) Front view before the excavation. (b) Cross section before the excavation. (c) Front view after the excavation. (d) Cross section after the excavation.

[26–28] are depicted in Figure 5. After the peak strength, the curves eventually switch to a stable stage which represents the residual strength. The tests conducted are reviewed and listed in Table 1. The ratio of residual strength to peak strength ranges from 0.15 to 0.38 with the average value of 0.25. Therefore, here, a value equal to a quarter of the peak strength of the coal rib is used as the critical stress σ_b to determine the width of the broken coal rib l. By substituting σ_b into Equation (1), the width l can be expressed as

$$l = \frac{MA}{2\tan\varphi_0}\ln\left(\frac{\sigma_b + (C_0/\tan\varphi_0)}{(C_0/\tan\varphi_0) + (P_s/A)}\right), \quad (2)$$

where

$$\sigma_b = \frac{1}{4}\times\psi\times\sigma_{\mathrm{p}}, \quad (3)$$

in which σ_{p} is the peak strength of the small coal specimen and ψ is the coefficient of the scale effect. Thus, the lengths a and b of the model shown in Figure 3 can be expressed as

$$\begin{aligned} a &= W + 2l, \\ b &= L_0 + l, \end{aligned} \quad (4)$$

where W denotes the width of the heading entry.

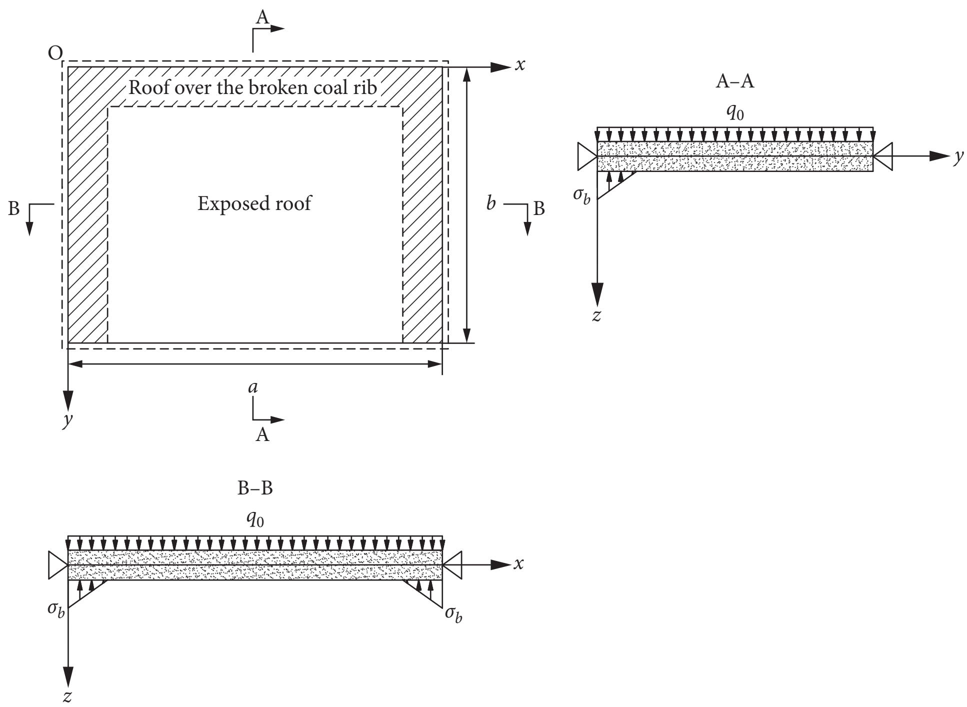

Figure 3: Simple supported rectangular plate model of the unsupported immediate roof.

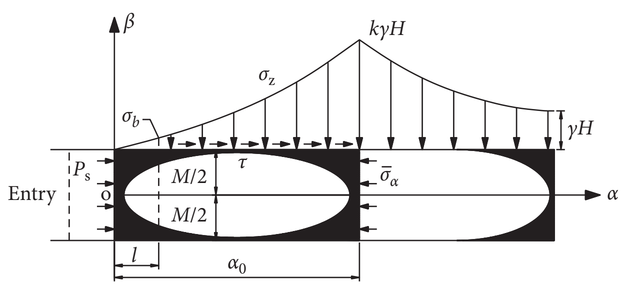

Figure 4: Model for calculating the normal stress distribution of the coal-roof interface of the coal rib.

3. Model Solution

The elastic thin plate theory [29] is used to solve the rectangular model proposed in Section 2. It avoids many complex settings and produces results that meet practical engineering requirements. The deflection of the model in Figure 3 can be expressed as

$$\omega = \sum_{m=1}^{\infty} \sum_{n=1}^{\infty} A_{mn} \sin \frac{m\pi x}{a} \sin \frac{n\pi y}{b}, \tag{5}$$

where

$$A_{mn} = \frac{q_{mn}}{D\pi^4 \left((m^2/a^2) + (n^2/b^2) \right)^2}, \tag{6}$$

$$q_{mn} = \frac{4}{ab} \int_0^a \int_0^b q(x, y) \sin \frac{m\pi x}{a} \sin \frac{m\pi y}{b} \, dx \, dy, \tag{7}$$

in which $q(x, y)$ denotes the load concentration. D represents the bending rigidity and can be expressed as

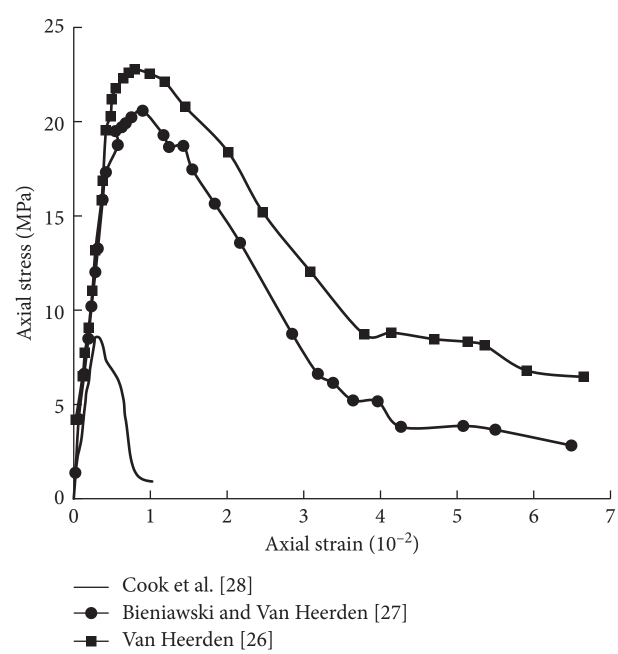

Figure 5: Complete stress-strain curve obtained for large-scale tests on coal.

$$D = \frac{Eh^3}{12(1 - \nu^2)}, \tag{8}$$

where E is the elastic modulus, h is the plate thickness, and ν is Poisson's ratio.

The bending moments M_x and M_y and the shear forces Q_x and Q_y are given as

Table 1: Summary of large-scale in situ tests.

Investigators	Cross section (cm)	Height (cm)	Peak strength (MPa)	Residual strength (MPa)	Ratio	Average
Van Heerden [26]	140 × 140	43	22.78	8.66	0.38	
Bieniawski and Van Heerden [27]	140 × 140	54	20.58	4.72	0.23	0.25
Cook et al. [28]	125 × 104	170	8.58	1.26	0.15	

$$\begin{aligned} M_x &= -D\left(\frac{\partial^2\omega}{\partial x^2}+v\frac{\partial^2\omega}{\partial y^2}\right),\\ M_y &= -D\left(\frac{\partial^2\omega}{\partial y^2}+v\frac{\partial^2\omega}{\partial x^2}\right),\\ Q_x &= -D\frac{\partial}{\partial x}\nabla^2\omega,\\ Q_y &= -D\frac{\partial}{\partial y}\nabla^2\omega. \end{aligned} \tag{9}$$

The maximum values of the normal stresses σ_x and σ_y appear on the surface of the plate, while the maximum values of the shear stresses τ_{xz} and τ_{xz} appear on the middle plane of the plate. They are given as

$$\begin{aligned} (\sigma_x)_{\max} &= \pm\frac{6M_x}{h^2},\\ \left(\sigma_y\right)_{\max} &= \pm\frac{6M_y}{h^2},\\ (\tau_{xz})_{\max} &= \frac{3}{2}\frac{Q_x}{h},\\ \left(\tau_{yz}\right)_{\max} &= \frac{3}{2}\frac{Q_y}{h}. \end{aligned} \tag{10}$$

The loads applied on the mechanical model depicted in Figure 3 are the overburden pressure and the coal-rib support pressure. Solving the model using the above equations directly is complicated and difficult. However, according to the superposition principle, the overall load q is equivalent to the superposition of the loads illustrated in Figure 6.

The overburden pressure q_0 is evenly distributed and can be expressed as

$$q_0 = \gamma\times h_{\mathrm{i}}, \tag{11}$$

where γ is denoted as the average unit weight of the overlying strata and h_{i} denotes the thickness of the immediate roof.

Compared to the overburden pressure q_0, the distribution range of the coal-rib support pressures q_{L}, q_{R}, and q_{F} is narrow. Hence, to simplify the calculation, the expressions of q_{L}, q_{R}, and q_{F} are simplified as linear relations, yielding

$$q_{\mathrm{L}} = \sigma_b\left(\frac{x}{l}-1\right),\quad 0\le x\le l,\ x\le y\le b, \tag{12}$$

$$q_{\mathrm{R}} = \sigma_b\left(\frac{a}{l}-\frac{x}{l}-1\right),\quad a-l\le x\le a,\ a-x\le y\le b, \tag{13}$$

$$q_{\mathrm{F}} = \sigma_b\left(\frac{y}{l}-1\right),\quad y<x\le a-y,\ 0\le y\le l. \tag{14}$$

Substituting Equations (11)–(14) into Equation (7) yields

$$q_{mn}^{0} = \frac{4\gamma h_i}{mn\pi^2}\left[(-1)^m-1\right]\left[(-1)^n-1\right], \tag{15}$$

$$\begin{aligned} q_{mn}^{L} = {} & \frac{4\sigma_b(-1)^{n+1}}{mn\pi^2}\left[\frac{a}{m\pi l}\sin\frac{m\pi l}{a}-1\right]\\ & -\frac{2b\sigma_b}{n\pi^2}\left\{\frac{2bm}{b^2m^2-a^2n^2}-\frac{ab}{(bm-an)^2\pi l}\sin\frac{(bm-an)\pi l}{ab}\right.\\ & \left.-\frac{ab}{(bm+an)^2\pi l}\sin\frac{(bm+an)\pi l}{ab}\right\}, \end{aligned} \tag{16}$$

$$\begin{aligned} q_{mn}^{R} = {} & \frac{4\sigma_b(-1)^{n+1}}{mn\pi^2}\left[(-1)^m+\frac{a}{m\pi l}\sin\frac{m\pi(a-l)}{a}\right]\\ & +\frac{2b\sigma_b}{n\pi^2}\left\{\frac{2bm(-1)^m}{b^2m^2-a^2n^2}+\frac{ab}{(bm-an)^2\pi l}\right.\\ & \cdot\sin\pi\left[\frac{(bm-an)(a-l)+a^2n}{ab}\right]\\ & \left.+\frac{ab}{(bm+an)^2\pi l}\sin\pi\left[\frac{(bm+an)(a-l)-a^2n}{ab}\right]\right\}, \end{aligned} \tag{17}$$

$$\begin{aligned} q_{mn}^{F} = {} & \frac{2a^2\sigma_b}{m\pi^2}\left\{\frac{2n\left[(-1)^m-1\right]}{a^2n^2-b^2m^2}+\frac{b\left[(-1)^m+1\right]}{(an+bm)^2\pi l}\right.\\ & \left.\cdot\sin\frac{(an+bm)\pi l}{ab}+\frac{b\left[(-1)^m+1\right]}{(an-bm)^2\pi l}\sin\frac{(an-bm)\pi l}{ab}\right\}. \end{aligned} \tag{18}$$

Then, inserting Equations (15)–(18) into Equations (5) and (6) gives ω_0, ω_{L}, ω_{R}, and ω_{F}. Finally, the deflection of the model in Figure 3 can be expressed as

$$\omega = \omega_0+\omega_{\mathrm{L}}+\omega_{\mathrm{R}}+\omega_{\mathrm{F}}. \tag{19}$$

4. Case Study

A real coal entry was selected as a case study to test and verify the theoretical model presented above. The example is tailgate entry no. 12311 serving for coal seam no. 11-2 extraction in the Panyi Mine, Huainan Mining Industry Group Co., Ltd., Anhui Province, China. The site was chosen because the Panyi Mine is suffering the extremely low-efficiency heading of coal entry, with an average heading

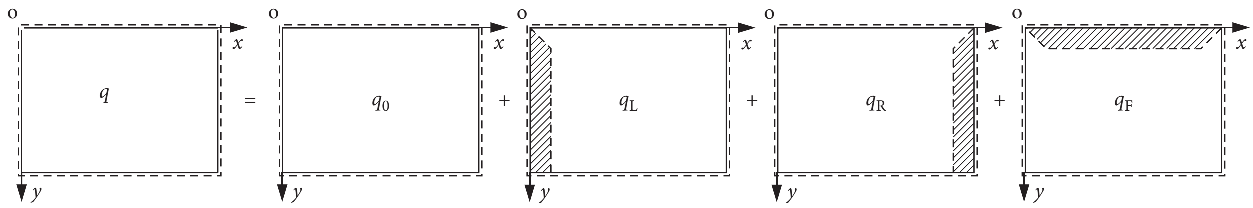

Figure 6: Decomposition of the overall load q.

rate of 220 m/month. The main reason for the slow rate is the short advancing distance (an average of 1 m) and the corresponding frequent position exchange of the machinery.

4.1. Geological Setting. Coal seam no. 11-2 is buried at an average depth of 760 m, and its average thickness is 2.4 m. Tailgate entry no. 12311 is cut as 2.1–2.4 m high and 5 m wide and is oriented N83°W. A geologic column of the mine roof obtained from a vertical core hole drilled at the site is shown in Figure 7. The roof may be roughly divided into three units:

(i) A slightly stronger siltstone layer in the lowest 1.1 m, comprising the immediate roof

(ii) A sequence of coal, weak claystone, and slickensided shale layers from 1.1 m to 14.4 m

(iii) A significantly stronger sandstone above 14.4 m, comprising the main roof

The properties of the coal ribs for the model in Section 3 were obtained from previous tests on coal from the adjacent Xieyi Mine [30]. The coal specimens taken from the Xieyi Mine were subjected to multistage triaxial testing, and the results are presented in Table 2. By using the linear Mohr–Coulomb criterion, the cohesion and friction angle of the coal specimens were determined as 7.92 MPa and 27°, respectively. The uniaxial strength and cohesion of the coal specimens cannot be directly recognized as the in situ properties of the coal ribs. However, by in situ large-scale coal testing, Bieniawski [31] found that the coefficient of the scale effect ψ can be set as 0.17. Accordingly, the in situ compressive strength and cohesion of the coal ribs used in the model were 3.91 MPa and 1.35 MPa, respectively.

As illustrated in Figure 2, our model ignored the bearing capacity of weak formations between the main roof and immediate roof and regarded them as the load applied on the immediate roof. By doing this, the calculation process has been greatly simplified; meanwhile, the safety margin of results can be increased. In order to understand the mechanical properties of the immediate roof of tailgate entry no. 12311, a series of tests were conducted on siltstone specimens obtained from the roof core (Figure 8): uniaxial compressive tests, Brazilian disc tests, and shear-compression tests. The results are presented in Tables 3–5, respectively. The relationship between the average shear strength and normal stress is illustrated in Figure 9. Based on the Mohr–Coulomb criterion, the cohesion and friction angle of the siltstone were derived as 4.86 MPa and 35.6°, respectively.

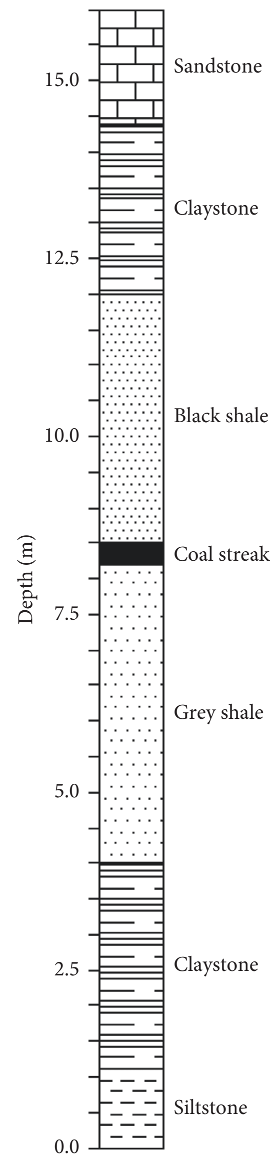

Figure 7: Composite core log from the study site showing the stratigraphy above the tailgate entry.

Table 2: Results of conventional triaxial tests from Reference [33].

No.	Confining pressure (MPa)	Peak strength (MPa)
1	0	22.99
2	10	61.65
3	20	87.03
4	30	113.14
5	40	135.66
6	50	156.41

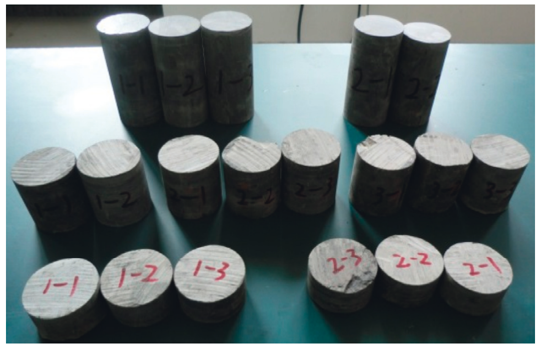

Figure 8: Siltstone specimens from the roof core prepared for the tests.

Table 3: Results of the uniaxial compressive test.

No.	Peak strength (MPa)	Average strength (MPa)	Elastic modulus (GPa)	Average modulus (GPa)	Poisson's ratio	Average ratio
1	29.97		3.16		0.21	
2	24.56		2.72		0.22	
3	22.19	25.36	2.36	2.66	0.24	0.22
4	21.30		2.61		0.23	
5	28.78		2.45		0.21	

Table 4: Results of the Brazilian disc test.

No.	Tensile strength (MPa)	Average tensile strength (MPa)
1	1.72	
2	2.80	
3	1.65	
4	2.02	2.18
5	2.35	
6	2.56	

Table 5: Results of the shear-compression test.

No.	Shear angle (°)	Normal stress (MPa)	Average normal stress (MPa)	Shear strength (MPa)	Average shear strength (MPa)
1	55	6.73		9.61	
2	55	6.29	6.76	8.98	9.65
3	55	7.25		10.35	
4	60	5.08	4.88	8.81	8.45
6	60	4.67		8.09	
7	65	3.49		7.49	
8	65	2.95	3.36	6.33	7.20
9	65	3.63		7.79	

The stress field was measured in two locations in haulage entry no. 12311 and adjacent recovery room no. 12521 (Figure 10). The results are shown in Table 6. By decomposing the principal stresses and extracting the stress vector in the direction perpendicular to tailgate entry no. 12311, the coefficient of horizontal stress A can be obtained as 0.9. The average unit weight of the overlying strata γ can be expressed as

$$\gamma = \frac{\overline{\sigma}_{\mathrm{v}}}{H}, \tag{20}$$

where $\overline{\sigma}_{\mathrm{v}}$ is the average vertical stress and H is the mining depth. Substituting the measurements in Table 5 into Equation (20), γ is obtained as 26836 N/m^3.

4.2. Results and Discussion. In Section 4.1, the detailed parameters describing the geological conditions of tailgate entry no. 12311 were determined by experimental and in situ tests. To study the roof stability at the heading face in tailgate entry no. 12311, we substituted these parameters into the

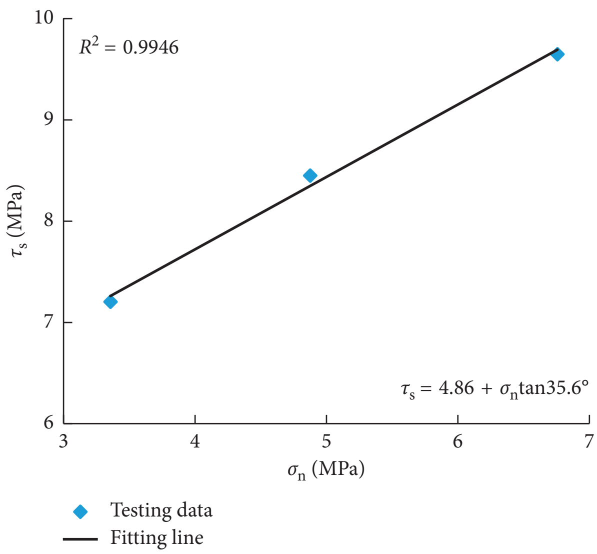

FIGURE 9: Average shear strength vs. average normal stress for siltstone.

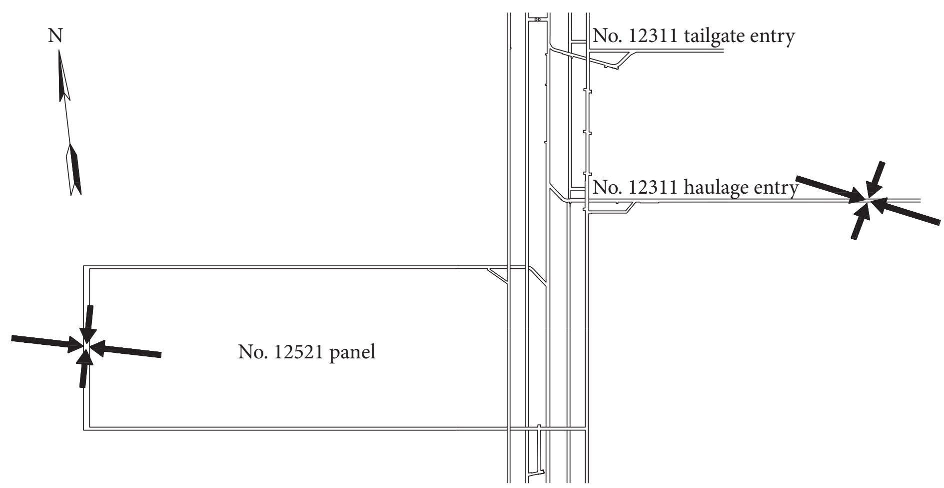

FIGURE 10: Principal stress distribution at the study sites.

model proposed in Section 3. Given the complexity of solving the equations, the commercial math software MATLAB R2012a (MathWorks, Inc., Natick, USA) was used.

As the first step to explore the possibility of increasing the advancing distance, the stress state of the current unsupported immediate roof (1 m long and 5 m wide) was analyzed. The distributions of the deflection, maximum normal stresses σ_x and σ_y, and maximum shear stresses τ_{xz} and τ_{yz} in the immediate roof are illustrated in Figure 11. The deflection is on a scale of decimillimetre; hence, it cannot be perceived by miners working in the heading face. The distribution of σ_x forms a hump-shaped pattern, with the two peaks located on the midline of the unsupported roof (Figure 11(b)). But the maximum value is only 0.137 MPa which is far below the tensile strength of the immediate roof (2.18 MPa). At this low stress level, the lateral broken coal ribs support the unsupported roof to some extent, which produces the bilateral compressive areas presented in Figure 11(b). Compared to the maximum normal stress σ_x, σ_y (Figure 11(c)) is relatively large, reaching a peak value of 0.486 MPa at the center of the unsupported roof. As the stress level rises, the supporting effect of the broken ribs weakens. The distribution of the maximum shear stress τ_{xz} (Figure 11(d)) shows two high-stress areas which are asymmetric, both along the lateral coal ribs. The maximum shear stress τ_{yz} (Figure 11(e)) has two high-stress areas at the front and back edges. The stress along the back edge which is corresponding to the row of bolts next to the heading face is more concentrated. The peak values of τ_{xz} and τ_{yz} are 0.152 MPa and 0.373 MPa, respectively. They are both small compared with the shear strength of the immediate roof. Overall, the results indicate that the midline, center, bilateral edges, and back edge of the unsupported immediate roof are possible failure areas, and more importantly, they confirm that the stress state of the current immediate roof is below

Table 6: Results of stress field measurements.

Site	Principal stress	Value (MPa)	Dip angle (°)	Azimuth angle (°)
12311	σ_1	35.82	20.5	114.3
	σ_2	20.38	67.5	320.3
	σ_3	18.39	9.1	207.7
	σ_v	20.99	0	—
12521	σ_1	36.11	11.5	103.5
	σ_2	19.13	77.7	263.4
	σ_3	18.07	4.1	12.7
	σ_v	19.80	0	—

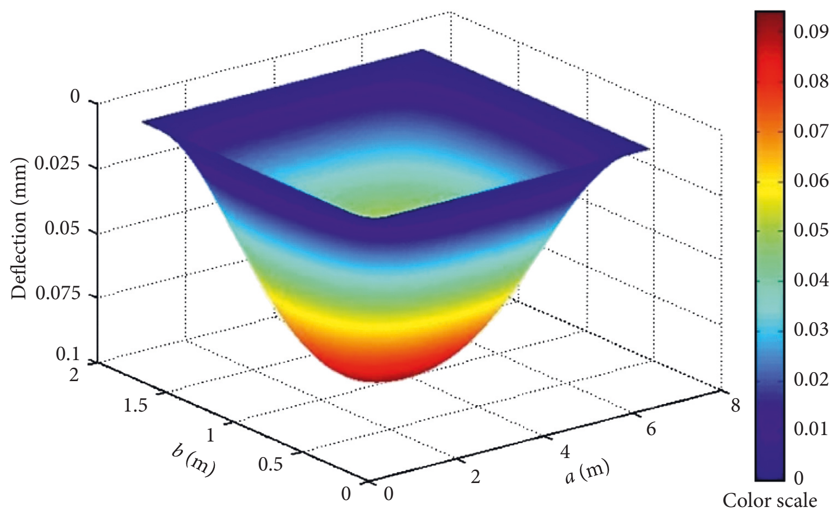

(a)

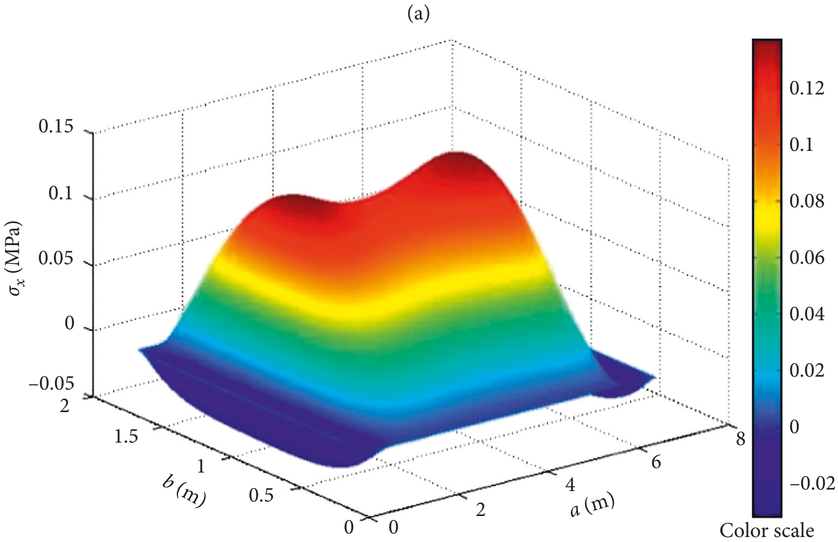

(b)

Figure 11: Continued.

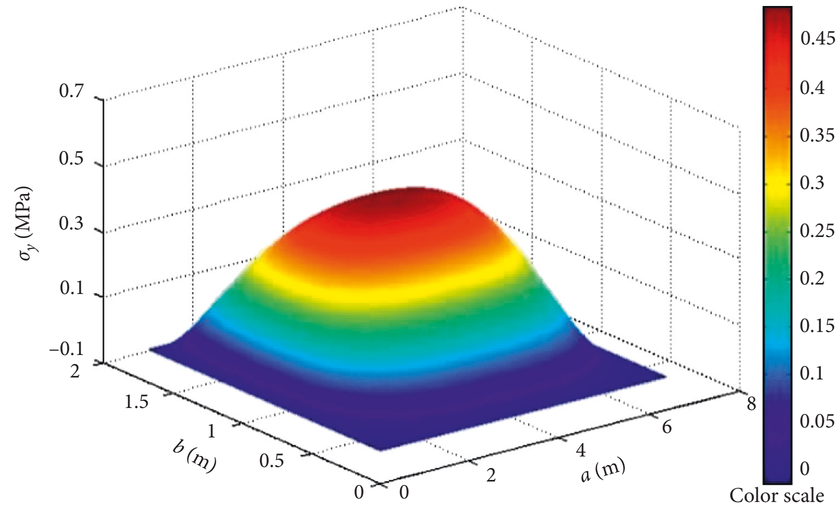

(c)

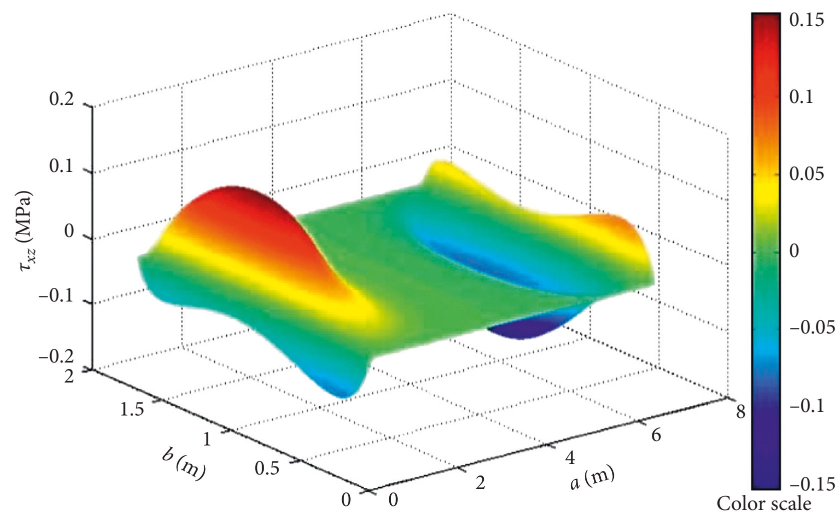

(d)

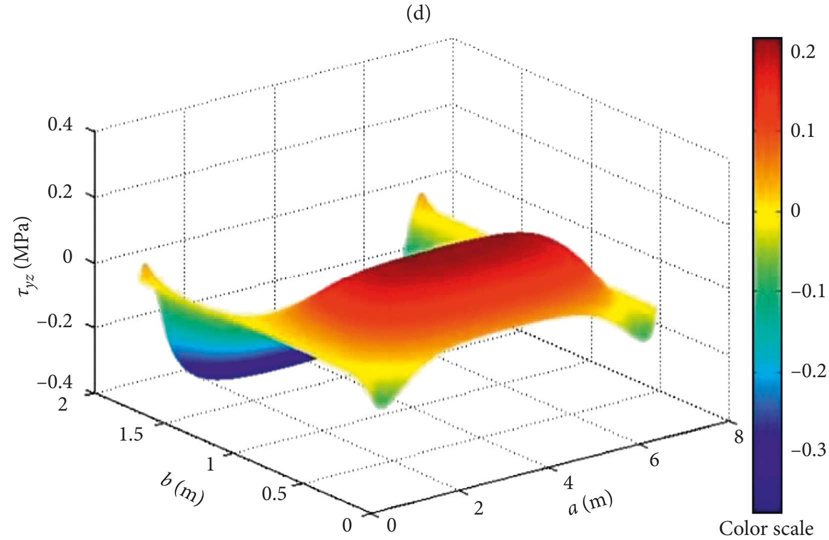

(e)

Figure 11: The mechanical state of the current unsupported immediate roof (1 m long and 5 m wide). (a) Distribution of deflection. (b) Distribution of normal stress σ_x. (c) Distribution of normal stress σ_y. (d) Distribution of shear stress τ_{xz}. (e) Distribution of shear stress τ_{yz}.

the threshold level needed to trigger the roof failure; thus, there is a large potential to increase the advancing distance.

To investigate the stress evolution characteristics of the unsupported immediate roof with the increasing advancing distance, we conducted a serial of calculations. The results were plotted against advancing distance and are shown in Figure 12. The peak value of deflection shows a nonlinear increase with the increasing advancing distance, but it is still on a scale of millimetre which is hard to measure or observe. The normal stress and shear stress show clearly different trends. Specifically, the peak values of σ_x and σ_y both rise with the increasing advancing distance, but σ_y reaches the tensile strength within a shorter range than σ_x. Moreover, the peak values of τ_{xz} and τ_{yz} initially increase with the increasing advancing distance and then become stable or decline. The simulation was designed to test whether the shear stress can reach the minimum shear strength determined as 4.86 MPa in Section 4.1. However, as depicted in Figures 12(d) and 12(e), it is far below the minimum shear strength even at an unrealistic length of advancing distance (29 m).

According to the above analysis, it is apparent that the major threat to roof stability at the heading face is tensile failure parallel to the heading direction. However, a problem arises from the determination of the tensile strength of the immediate roof. Since the coal mine roof is commonly disturbed by faults, beddings, and joints, its strength cannot be equated to the strength derived from the small rock sample. Therefore, a reduction parameter is required to relate the roof strength to the rock strength in the laboratory. So far, extensive works have been devoted to this issue; several rock mass classification systems (for e.g., RMR [32], MRMR [33], Q-system [34], and GSI [35]) have been established and successfully applied in engineering practice, but the fairly high time cost is a major shortcoming of these classification systems blocking their application to this study. As mentioned, the main intention of the establishment of the foregoing analytical method is to increase the efficiency of coal entry heading. However, the previous rock mass classification systems generally need a variety of input parameters (joint spacing, joint roughness, water reduction factor, etc.), some of which are based on the time-consuming in situ observation and borehole logging. Besides, these classification systems are not designed to rate the roof impacted by a variable geological condition; hence, parameter adjustments are required to be continuously conducted with the advance of heading, which would greatly slow down the heading rate. In view of the problem, a simplified but competent relationship between roof strength and laboratory rock strength is necessary to allow the further analysis.

The existing empirical relations of in situ deformation modulus and rock quality designation (RQD) paved a way for overcoming the problem because of the following reasons:

(1) The positive correlation between rock mass strength and deformation modulus has been proven by numerous researchers [36–38]; therefore, it becomes convenient to relate the rock mass strength to RQD.

(2) Compared to the rock mass strength, the dataset of the deformation modulus of rock mass is much larger, which can be attributed to the utilization of the seismic technique in its determination. A larger dataset indicates a more reliable relation.

(3) RQD is a single parameter and can be easily calculated from core drilling; this simplicity makes it possible to evaluate the variable condition of the immediate roof.

Zhang and Einstein [39] collected about 120 sets of published data covering mudstone, siltstone, sandstone, shale, dolerite, granite, limestone, greywacke, gneiss, and granite gneiss and derived an empirical relation between the modulus reduction ratio $E_{\mathrm{m}}/E_{\mathrm{i}}$ and the RQD:

$$\frac{E_{\mathrm{m}}}{E_{\mathrm{i}}} = 10^{0.0186\mathrm{RQD}-1.91}, \tag{21}$$

where E_{m} and E_{i} are the deformation moduli of the rock mass and the intact rock, respectively. The reduction ratio of deformation modulus is employed to relate the roof strength to the laboratory-scale rock strength. Based on RQD, the immediate roof conditions are classified into four types and presented in Table 7. To increase the safety margin, the reduction ratio (R_{s}) of each type is calculated by substituting the lower value of RQD into Equation (21). Subsequently, R_{s} is introduced into the calculation of the advancing distance in heading of tailgate entry no. 12311. The critical tensile stress $(\sigma_y)_{\mathrm{c}}$ below which the immediate roof can maintain self-stability is given as

$$\left(\sigma_y\right)_{\mathrm{c}} = R_{\mathrm{s}} \times T, \tag{22}$$

where T is the tensile strength of the small sample drilled from the immediate roof and has been determined as 2.18 MPa in Table 4. The determined $(\sigma_y)_{\mathrm{c}}$ of each roof condition type is presented in Table 7.

It can be observed in Figure 12 that the tensile stress parallel to the heading direction (σ_y) exhibits the fastest increase with the increasing advancing distance. Therefore, the advancing distance of each type of roof condition is determined by substituting their critical tensile stress into the linear relationship presented in Figure 12(c). It has to be noted that the advancing distance of the roof condition with RQD lower than 70% is kept as the original value (1 m). Before applying the advancing distances to the entry heading, the expected mechanical state of the unsupported immediate roof was studied (an example of 1.9 m advancing distance is shown in Figure 13). The results confirm that the stress distributions are all within a safe level and indicate that the advancing distance in the modeled coal seam of the Panyi Mine can be confidently increased.

The expected length of tailgate entry no. 12311 is 1370.5 m. Before employing the newly designed advancing distance, the heading face had advanced 370 m taking 55 days. Thus, the average heading rate was 202 m/month. After

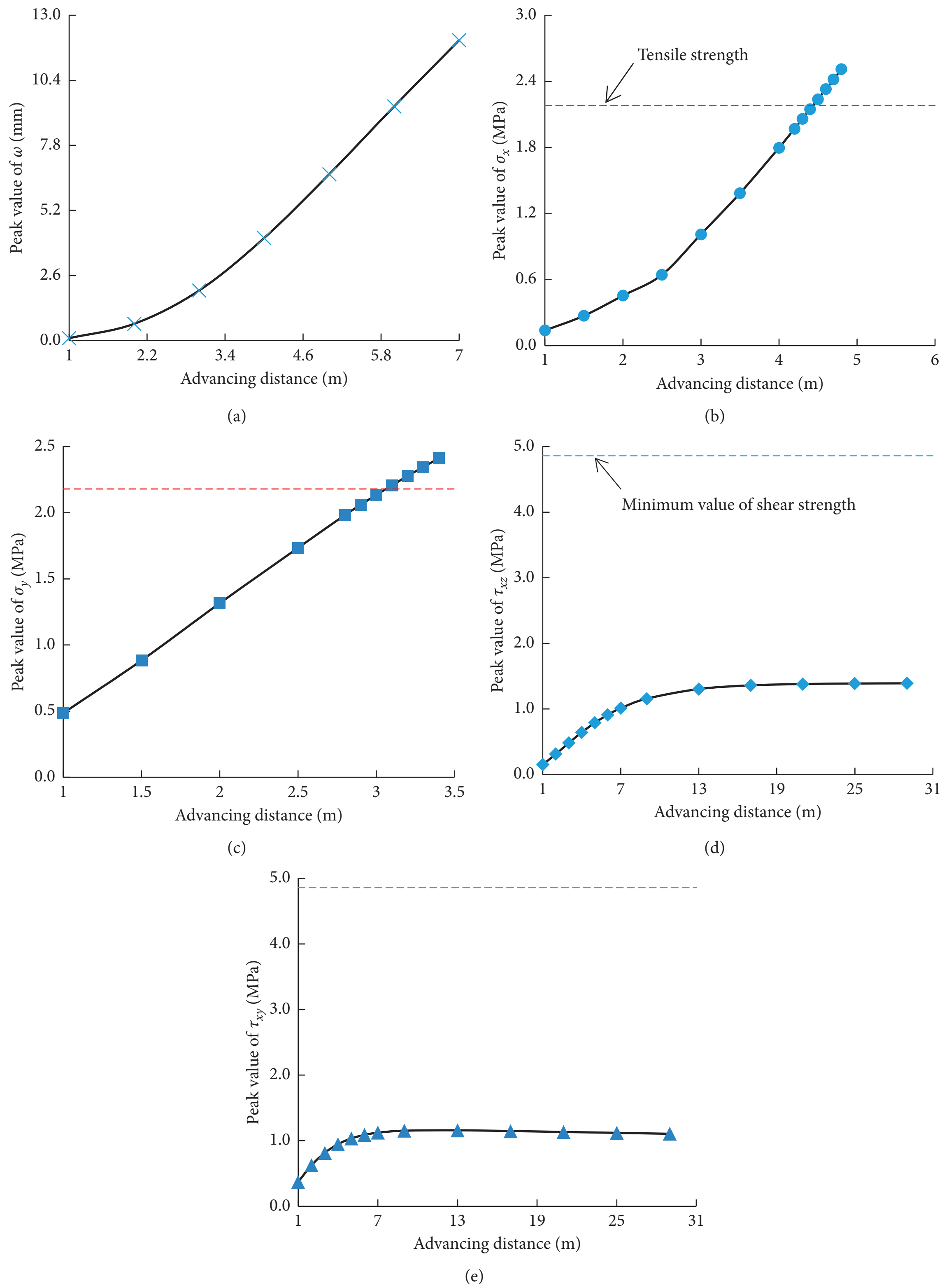

FIGURE 12: Evolution of the mechanical state of the unsupported immediate roof with the increasing advancing distance. (a) Peak value of deflection vs. advancing distance. (b) Peak value of σ_x vs. advancing distance. (c) Peak value of σ_y vs. advancing distance. (d) Peak value of τ_{xz} vs. advancing distance. (e) Peak value of τ_{yz} vs. advancing distance.

adopting the newly designed advancing distance, the remaining 1000.5 m was excavated in 74 days with no roof falls. Thus, even with a considerable safety margin, the heading rate was improved from 202 m to 406 m per month. The frequency of position changes between the roadheader and the roof bolter decreased from 6.7/day to 5.4/day, which

Table 7: Results of the calculation of the advancing distance in heading of tailgate entry no. 12311.

No.	RQD range (%)	Strength reduction ratio	Critical tensile stress (MPa)	Advancing distance (m)
1	90~100	0.58	1.26	1.9
2	80~90	0.38	0.83	1.4
3	70~80	0.25	0.55	1.1
4	<70	—	—	1

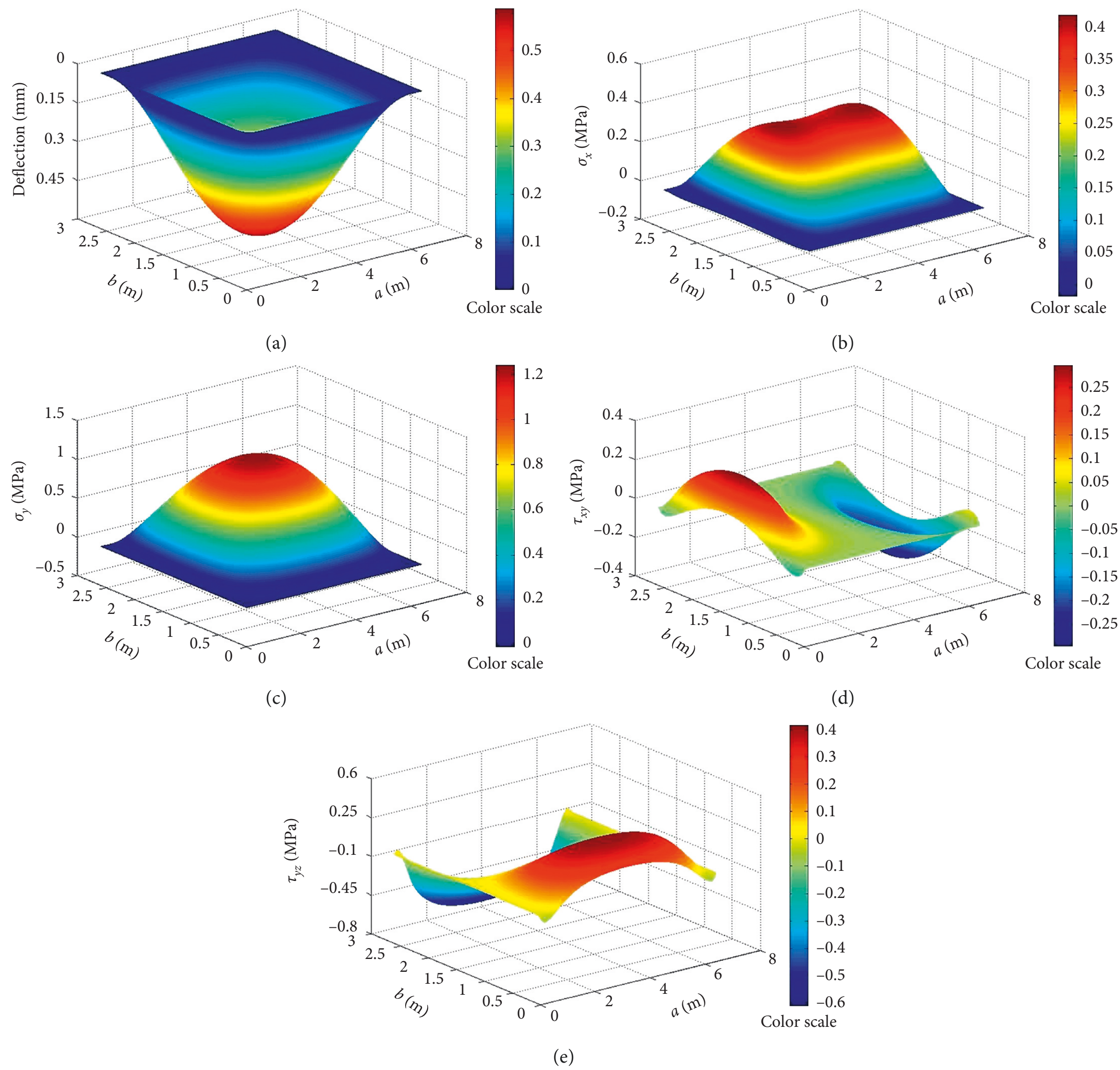

Figure 13: The mechanical state of the simulated unsupported immediate roof with the extended advancing distance (1.9 m long and 5 m wide). (a) Distribution of deflection. (b) Distribution of normal stress σ_x. (c) Distribution of normal stress σ_y. (d) Distribution of shear stress τ_{xz}. (e) Distribution of shear stress τ_{yz}.

reduced the labor intensity. Finally, the proposed method was verified as a reliable method for predicting the mechanical state of the unsupported immediate roof, providing a safe and effective tool to help achieve highly efficient heading of coal entry.

5. Conclusions

This study focuses on developing a systematic method to predict the mechanical behavior of the unsupported immediate roof and preventing roof collapse while pursuing the highly efficient heading of coal entry. The theoretical model was applied to data collected from a Chinese coal mine. Based on the results, the following conclusions were drawn:

(1) The deflection of the unsupported immediate roof at the heading face was on a scale of millimetre; hence, it is difficult to monitor the deformation of the unsupported immediate roof using conventional observation methods. It is thus extremely dangerous to determine the extent of safe advancing distance by observing the deformation of the unsupported immediate roof.

(2) The proposed model shows that the peak values of normal stress and shear stress in the unsupported immediate roof show different changing trends. The peak values of σ_x and σ_y both rise with the increasing advancing distance, while σ_y reaches the tensile strength within a shorter range than σ_x. Moreover the peak values of τ_{xz} and τ_{yz} initially increase with the increasing advancing distance and then stabilize or decline.

(3) The peak values of τ_{xz} and τ_{yz} cannot reach the minimum shear strength over the range of advancing distance from 1 m to 29 m. Therefore, shear failure is unlikely to occur in the unsupported immediate roof.

(4) The major cause of roof instability at the heading face is tensile failure parallel to the heading direction.

(5) Based on engineering practice, the theoretical method was verified as a reliable model for predicting the mechanical state of the unsupported immediate roof and can be used confidently to achieve safe and highly efficient heading of coal entry.

Data Availability

The data used to support the findings of this study are available from the corresponding author upon request.

Conflicts of Interest

The authors declare that they have no conflicts of interest.

Acknowledgments

This work was supported by the Fundamental Research Funds for the Central Universities (2018BSCXC31) and Postgraduate Research & Practice Innovation Program of Jiangsu Province (KYCX18_1963).

References

[1] Q. Zhang, J. X. Zhang, Y. L. Huang, and J. Feng, "Backfilling technology and strata behaviors in fully mechanized coal mining working face," *International Journal of Mining Science and Technology*, vol. 22, no. 2, pp. 151–157, 2012.

[2] X. Feng, N. Zhang, L. Gong, F. Xue, and X. Zheng, "Application of a backfilling method in coal mining to realise an ecologically sensitive "black gold" industry," *Energies*, vol. 8, no. 5, pp. 3628–3639, 2015.

[3] H. Liu, Y. Cheng, H. Zhou, W. Wang, and H. Zhang, "Guidance and control effect of drawing speed on excellent gas channel at fully mechanized longwall face," *Journal of China Coal Society*, vol. 40, pp. 809–815, 2015.

[4] J. Yang, S. Sun, and D. Kong, "Effect of working face length and advancing speed on strata behaviors in high-intensity mining," *Rock and Soil Mechanics*, vol. 36, pp. 334–339, 2015.

[5] G. M. Molinda, C. Mark, and D. Dolinar, "Assessing coal mine roof stability through roof fall analysis, new technology for coal mine roof support," in *Proceedings of NIOSH Open Industry Briefing, NIOSH IC*, pp. 53–72, 2000.

[6] J. van der Merwe, J. Van Vuuren, R. Butcher, and I. Canbulat, "Causes of falls of roof in South African collieries," South Africa Final Project Report No. COL613, SIMRAC, Department of Minerals and Energy, Johannesburg, South Africa, 2001.

[7] G. M. Molinda, *Geologic Hazards and Roof Stability in Coal Mines*, US Department of Health and Human Services, Public Health Service, Centers for Disease Control and Prevention, National Institute for Occupational Safety and Health, Pittsburgh Research Laboratory, Washington, DC, USA, 2003.

[8] D. Deb, "Analysis of coal mine roof fall rate using fuzzy reasoning techniques," *International Journal of Rock Mechanics and Mining Sciences*, vol. 40, no. 2, pp. 251–257, 2003.

[9] C. Mark and G. Molinda, "The coal mine roof rating (CMRR)—a decade of experience," *International Journal of Coal Geology*, vol. 64, no. 1-2, pp. 85–103, 2005.

[10] S. Palei and S. Das, "Sensitivity analysis of support safety factor for predicting the effects of contributing parameters on roof falls in underground coal mines," *International Journal of Coal Geology*, vol. 75, no. 4, pp. 241–247, 2008.

[11] S. K. Palei and S. K. Das, "Logistic regression model for prediction of roof fall risks in bord and pillar workings in coal mines: an approach," *Safety Science*, vol. 47, no. 1, pp. 88–96, 2009.

[12] E. Ghasemi, M. Ataei, K. Shahriar, F. Sereshki, S. E. Jalali, and A. Ramazanzadeh, "Assessment of roof fall risk during retreat mining in room and pillar coal mines," *International Journal of Rock Mechanics and Mining Sciences*, vol. 54, pp. 80–89, 2012.

[13] P. K. Kaiser, "Monitoring for the evaluation of the stability of underground openings," in *Proceedings of 1st Conference on Ground Control in Mining*, pp. 90–97, West Virginia University, Morgantown, WV, USA, July 1981.

[14] V. Hucka and S. Singh, "Geological aspects of stability in underground coal mines," in *Proceedings of 1st AIME-SME International Conference on Stability in Underground Mining*, pp. 165–180, Vancouver, Canada, August 1982.

[15] J. Tennant, "Methods used to monitor roof geology and entry supports," in *Proceedings of 2nd Conference on Ground Control in Mining*, pp. 118–122, West Virginia University, Morgantown, WV, USA, July 1982.

[16] M. Karmis and W. Kane, "An analysis of the geomechanical factors influencing coal mine roof stability in Appalachia," in *Proceedings of the Second International Conference on Stability in Underground Mining*, pp. 311–328, Lexington, KY, USA, August 1984.

[17] A. D. Smith, "Relationships of assumed condition of mine roof and the occurrence of roof falls in eastern Kentucky coal fields," in *Proceedings of 2nd International Conference on*

Stability in Underground Mining, pp. 329–345, Lexington, KY, USA, August 1984.

[18] J. Shepherd, K. L. Rixon, and K. P. Walton, "Borescope techniques for assisting colliery roof control," in *Proceedings of Symposium on Ground Movement and Control Related to Coal Mining*, pp. 32–40, August 1986.

[19] S. Greb and J. Cobb, "Geologic classification and modeling of potential roof control problems in underground coal mines," in *Proceedings of Multinational Conference on Mine Planning and Design*, pp. 27–32, Lexington, KY, USA, April 1989.

[20] J. B. Bai, T. J. Xiao, and L. Li, "Unsupported roof distance determination of roadway excavation using difference method and its application," *Journal of China Coal Society*, vol. 36, pp. 920–924, 2011.

[21] J. Coggan, F. Gao, D. Stead, and D. Elmo, "Numerical modelling of the effects of weak immediate roof lithology on coal mine roadway stability," *International Journal of Coal Geology*, vol. 90-91, pp. 100–109, 2012.

[22] F. Gao and D. Stead, "Discrete element modelling of cutter roof failure in coal mine roadways," *International Journal of Coal Geology*, vol. 116-117, pp. 158–171, 2013.

[23] X. Su, X. Song, H. Li, H. Yuan, and B. Li, "Study on coupled arch-beam support structure of roadway with extra-thick soft compound roof," *Chinese Journal of Rock Mechanics and Engineering*, vol. 33, no. 9, pp. 1828–1836, 2014.

[24] M. Ji, H. Guo, H. Liu, Y. Zhang, L. Cheng, and G. Wang, "Stability control mechanism of mudstone wedge structure roof in crossing coal seam roadway," *Journal of Mining and Safety Engineering*, vol. 31, pp. 920–925, 2014.

[25] C. Hou and N. Ma, "Stress in in-seam roadway sides and limit equilibrium zone," *Journal of China Coal Society*, vol. 4, pp. 21–29, 1989.

[26] W. L. Van Heerden, "In situ complete stress-strain characteristics of large coal specimens," *Journal of the Southern African Institute of Mining and Metallurgy*, vol. 75, no. 8, pp. 207–217, 1975.

[27] Z. T. Bieniawski and W. L. Van Heerden, "The significance of in situ tests on large rock specimens," *International Journal of Rock Mechanics and Mining Sciences and Geomechanics Abstracts*, vol. 12, no. 4, pp. 101–113, 1975.

[28] N. G. W. Cook, K. Hodgson, and J. P. M. A. Hojem, "100-MN jacking system for testing coal pillars underground," *Journal of the Southern African Institute of Mining and Metallurgy*, vol. 71, no. 11, pp. 215–224, 1971.

[29] P. G. Lowe, *Elastic Plates. Basic Principles of Plate Theory*, Springer Science and Business Media, New York, NY, USA, 2012.

[30] Q. Liu, K. Liu, J. Zhu, and X. Lu, "Study of mechanical properties of raw coal under high stress with triaxial compression," *Chinese Journal of Rock Mechanics and Engineering*, vol. 33, pp. 24–34, 2014.

[31] Z. T. Bieniawski, "The effect of specimen size on compressive strength of coal," *International Journal of Rock Mechanics and Mining Sciences and Geomechanics Abstracts*, vol. 5, no. 4, pp. 325–335, 1968.

[32] Z. T. Bieniawski, "Engineering rock mass classifications: a complete manual for engineers and geologists in mining, civil and petroleum engineering," *Petroleum*, vol. 251, no. 3, pp. 357–365, 1989.

[33] D. H. Laubscher, "A geomechanics classification system for rating of rock mass in mine design," *Journal of the Southern African Institute of Mining and Metallurgy*, vol. 90, no. 10, pp. 257–273, 1990.

[34] N. Barton, "Some new Q-value correlations to assist in site characterisation and tunnel design," *International Journal of Rock Mechanics and Mining Sciences*, vol. 39, no. 2, pp. 185–216, 2002.

[35] E. Hoek and E. T. Brown, "Empirical strength criterion for rock masses," *Journal of the Geotechnical Engineering Division*, vol. 106, no. 9, pp. 1013–1035, 1982.

[36] N. A. Al-Shayea, "Effects of testing methods and conditions on the elastic properties of limestone rock," *Engineering Geology*, vol. 74, no. 1-2, pp. 139–156, 2004.

[37] H. Sonmez, E. Tuncay, and C. Gokceoglu, "Models to predict the uniaxial compressive strength and the modulus of elasticity for Ankara agglomerate," *International Journal of Rock Mechanics and Mining Sciences*, vol. 41, no. 5, pp. 717–729, 2004.

[38] V. Palchik, "On the ratios between elastic modulus and uniaxial compressive strength of heterogeneous carbonate rocks," *Rock Mechanics and Rock Engineering*, vol. 44, no. 1, pp. 121–128, 2011.

[39] L. Zhang and H. H. Einstein, "Using RQD to estimate the deformation modulus of rock masses," *International Journal of Rock Mechanics and Mining Sciences*, vol. 41, no. 2, pp. 337–341, 2004.


Journal of
Engineering
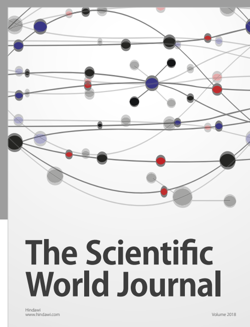
The Scientific World Journal
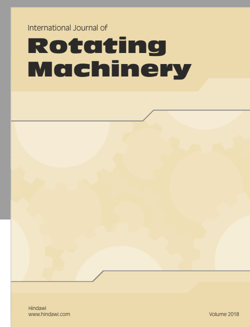
International Journal of
Rotating Machinery

Journal of
Sensors
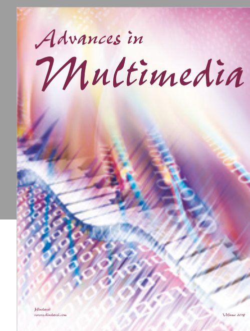
Advances in
Multimedia
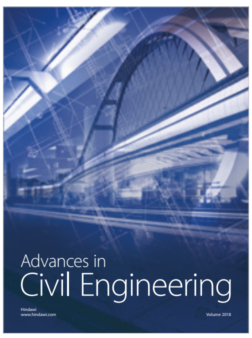
Advances in
Civil Engineering

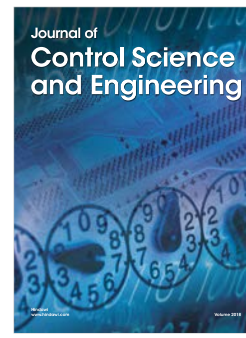
Journal of
Control Science and Engineering

Journal of
Robotics
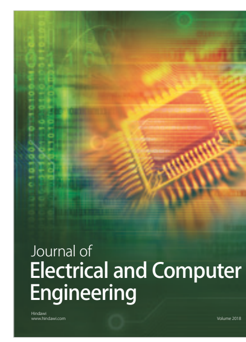
Journal of
Electrical and Computer Engineering
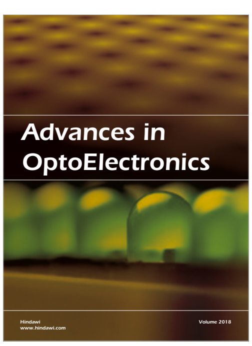
Advances in
OptoElectronics

VLSI Design

International Journal of
Navigation and Observation
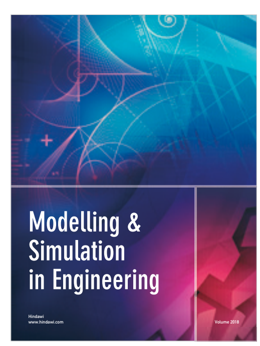
Modelling & Simulation in Engineering

International Journal of
Aerospace Engineering

International Journal of
Chemical Engineering
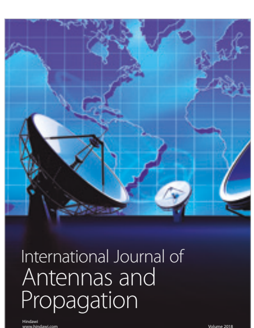
International Journal of
Antennas and Propagation

Active and Passive Electronic Components
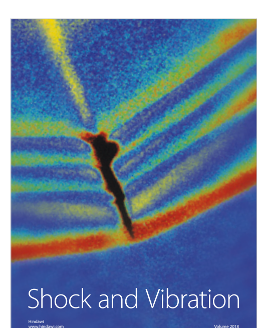
Shock and Vibration

Advances in
Acoustics and Vibration